IJE TRANSACTIONS A: Basics Vol. 39, No. 10, (October 2026) 2630-2643

International Journal of Engineering

Journal Homepage: www.ije.ir

Optimum design of a Novel Dual-PM Axial-Field Flux Reversal Machine for an In-wheel Direct-Drive Electric Vehicle Application

H. W. F. AL-Ward, S. E. Abdollahi*, S. A. Gholamian

Electrical and Computer Engineering Department, Babol Noshirvani University of Technology, Babol, Iran

P A P E R I N F O

Paper history:
Received 14 August 2025
Received in revised form 11 October 2025
Accepted 20 December 2025

Keywords:
Dual Permanent Magnet
Axial Field Flux Reversal Machine
Torque Density
Taguchi Method
Electric Vehicle

A B S T R A C T

This article presents a novel dual permanent magnet axial field flux reversal machine (dual-PM AFFRM) with a single stator and a single rotor for an In-wheel direct drive electric vehicle (EV) application. The topology and operation principle of the machine were explained, and the impacts of using dual PM configuration on the airgap flux density harmonics were revealed using a simple magnetomotive force (MMF)-permeance model. To obtain the optimum torque characteristic of the machine and reduce the computational effort, the Taguchi method is employed. The electromagnetic performances of the optimized design are assessed via the 3-D finite element method (FEM). The outcomes show that the optimized machine offers high torque capability, low torque ripple, and good flux weakening capability. In addition, the results of a comparative study among eight different traction machines reveal that the dual-PM AFFRM offers the highest torque density with high aspect ratio, and high torque constant, which are crucial for direct-drive In-wheel EV applications.

doi: *10.5829/ije.2026.39.10a.22*

Graphical Abstract

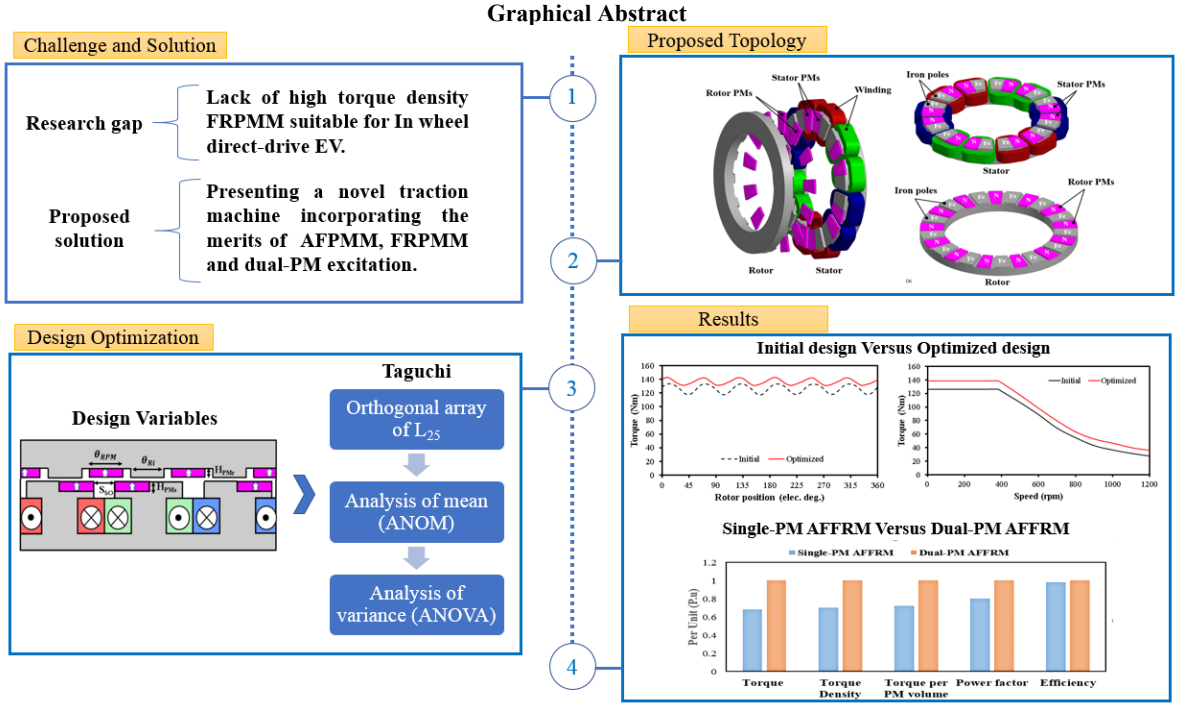

*Corresponding Author Email: e.abdollahi@nit.ac.ir (S. E. Abdollahi)

Please cite this article as: AL-Ward HWF, Abdollahi SE, Gholamian SA. Optimum design of a Novel Dual-PM Axial-Field Flux Reversal Machine for an In-wheel Direct-Drive Electric Vehicle Application. International Journal of Engineering, Transactions A: Basics. 2026;39(10):2630-43.

1. INTRODUCTION

Recently, Flux Reversal Permanent Magnet machine (FRPMM), due to its desired characteristics, is emerging as a promising choice for direct-drive applications (1). The conventional type of FRPMM employs a reluctance rotor, which makes it suitable for applications where mechanical robustness is an area of concern. In addition, with permanent magnets (PMs) mounted on its stator teeth, heat management is easier and less complex. Nevertheless, the root problem of conventional FRPMM is its relatively low torque density caused by a high leakage flux between adjacent PMs (2).

Various types of FRPMMs have been explored and investigated to improve the torque density. A consequent-pole (CP) arrangement of PMs is employed to reduce the leakage flux and PM volume as well as enhance the PM utilization ratio and torque density of a conventional FRPMM (2). The results showed that CP-FRPMM delivers 26% higher average torque compared to the conventional FRPMM. The effects of PM's position on the torque density in CP-FRPMM were investigated by Yang et al. (3) using biased flux modulation theory. Qu et al. (4) introduced a novel type of CP-FRPMM with a larger number of iron poles than PM poles, which can improve the torque capacity of the machine up to 40% in comparison with a conventional CP-FRPMM. In addition, the optimal number of PM pieces on one stator tooth (5), and the adjacent teeth's PM polarities (6) are further studied to increase torque density. Besides, adding a flux-focusing feature to conventional FRPMM is proven to be an effective way to elevate the torque capacity. In this regard, an inset-type FRPMM is developed and studied b Kimy (7). In addition, inserting a quasi-Halbach array PMs (8) and spoke array PMs (9, 10) into the stator slots of FRPMMs is further examined. It is revealed that placing PMs into the stator slots of conventional FRPMMs improves the magnetic loading and torque production capacity. Apart from different arrangements of PMs, other methods have been used to boost the performance of FRPMM. For example. A FRPMM with distributed winding presented by More and Fernandes (11) offers high power density and efficiency. Li et al. (12) proposed a FRPMM with todoidal winding to improve the low pitch factor, which is accompanied by the desired slot-pole combination in the conventional FRPMM with concentrated winding. Another approach to increase the torque density is the utilization of the space occupied by the reluctance rotor in the conventional FRPMM. It is realized by accommodating an auxiliary set of windings inside the rotor slots, turning the conventional type into a novel doubly-fed FRPMM (13-15). Also, the concept of utilizing the inner space of the rotor led to the development of FRPMMs with mechanical offset complementary-stator (16), double-stator with quasi-Halbach array PMs (17), dual-stator with triple-PM excitations (18), partitioned stator hybrid-excited with dual-PM (19), and different topologies of partitioned stator (20-22) in which PMs are moved to the inner stator.

Despite the considerable improvement in the torque performance of FRPMM, the figures in the previous studies are not satisfactory for some demanding applications. For example, in an electric vehicle (EV) with an In-wheel direct-drive system, the traction motor is required to deliver high torque at low speed within the confined space of the wheel. The existing numbers reported for the torque density of the traction motors suitable for small-sized electric vehicles range from 30.2 kNm/m^3 to 37.7 kNm/m^3 (23, 24). Meanwhile, findings by Qu et al. (4) and Wu et al. (22) showed torque density figures for low-speed high-torque FRPMMs to be 17.6 kNm/m^3 and 8.62 kNm/m^3, respectively. Although higher numbers can be obtained in some studies, like Wei et al. (25) reached around 36 kNm/m^3, the complex structure of the stator with a rather long axial length makes it unattractive for In-wheel direct-drive systems, where the structural integrity and short axial length are of utmost importance. Thus, further improvement of torque density is necessary for FRPMM to be a better fit for such applications.

So far, most of the research on FRPMMs has been carried out on radial-flux topologies. It is evidenced by plenty of research investigations that axial flux permanent magnet machines (AFPMMs) offer a higher torque density with a shorter axial length and compact size, making them a viable solution, especially for high-torque low-speed applications (24). Up to now, there is one study conducted on axial field flux reversal permanent magnet machine (AFFRPMM), focusing on torque ripple reduction (26). Therefore, to combine the merits of FRPMM with those of the AFPMMs, this paper presents a new dual-PM axial field flux reversal machine (dual-PM AFFRM) with a single stator and a single rotor for an in-wheel direct drive EV. The structure and operation principle of the proposed machine are illustrated and explained using a simple magnetomotive force (MMF)-permeance model in section 2. The proposed machine requires a 3-D finite element method (FEM) for optimization and performance analysis, which consumes a significant amount of time. To reduce the computational time and obtain the optimum design, the Taguchi method is used in this study, and its implementation is explained in section 3. The electromagnetic performances of the optimized design are presented in section 4. To assess the capabilities of the proposed machine, its performance is compared to that of the AFPMMs and radial-flux FRPMMs designed for low-speed and high-torque applications in section 5. Finally, the main characteristics of the proposed machine are concluded in section 5.

2. TOPOLOGY AND OPERATING PRINCIPLE

Figure 1 shows the exploded model of the proposed dual-PM AFFRM. The machine has a doubly salient structure, and the armature coils are wound around its stator teeth, forming a non-overlapping concentrated winding, which features a short end-winding and low copper loss (27-29). There are two sets of PMs mounted on the stator teeth as well as in the rotor slots. The stator exploits the CP arrangement of PMs with N-Fe/Fe-N order, where "Fes" are ferromagnetic teeth used to reduce the interpolar leakage flux and act as a modulator for the MMF produced by the rotor PMs. Similarly, the rotor is comprised of a CP arrangement of PMs where all the PMs have the same magnetization directions as those of the stator, while ferromagnetic teeth of the rotor operate both as the opposite poles for the rotor PMs and the modulator for the MMF produced by the stator PMS.

The working mechanism of the dual-PM AFFRM is explained by depicting the individual contribution of the stator and the rotor PM excitations to the flux linkage of the stator coil (indicated by the light green) as shown in Figure 2. As can be seen, when the rotor position is θe=0° electrical degree in Figure 2(a), the flux produced by both the PM excitations is short-circuited through the iron teeth of the stator and rotor, and the flux linkage of the coil is zero. As the rotor position changes to θe=90° electrical degree in Figure 2(b), the rotor tooth is aligned with the stator N pole, while the rotor N pole coincides with the stator tooth. As a result, the flux linkage of the coil reaches its positive maximum. It is clear that in this position, both the flux produced by the stator and the rotor PMs strengthen each other, leading to a higher flux linkage in the stator coil. In Figure 2(c), when the rotor position is at θe=180°, the flux of the stator and the rotor PMs is short-circuited and the net flux linkage of the coil drops to zero. In Figure 2(d), the rotor is displaced to θe=270° electrical degree where both the ferromagnetic teeth of the stator and rotor are aligned with each other, creating a path for the flux produced by both excitations.

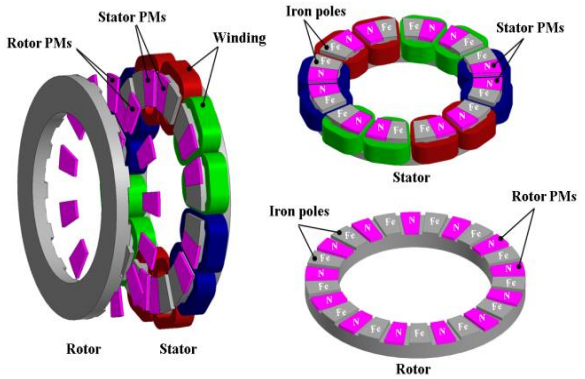

Figure 1. Topology of the proposed dual-PM AFFRM

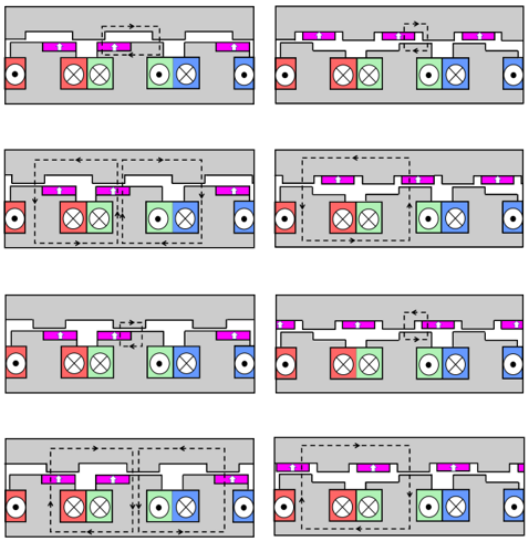

Figure 2. Flux lines of the dual-PM AFFRM. (a) θe=0°. (b) θe=90°. (c) θe=180°. (d) θe=270°

In this position, the flux linkage of the stator coil reaches its negative maximum. As analyzed the flux paths in different rotor positions, the proposed machine has a bipolar flux linkage which makes it suitable for BLAC operation mode.

For the presented dual-PM AFFRM, the magnetic field in the airgap is contributed by two different sources, namely the stator PM-MMF and the rotor PM-MMF. Considering the stator PMs only, the corresponding MMF can be expressed as follows (18):

$$F_{PMs}(\theta) = \sum_{n=1,3,5,\dots}^{\infty} F_{sn} \sin(n\frac{N_s}{2}\theta) \quad (1)$$

where N_s is the number of the stator slots, θ is the mechanical angle in the stator reference frame, and F_{sn} is the magnitude of the nth harmonic order of the MMF excited by the stator PMs (F_{PMs}). In addition, when the rotor PMs are only considered, the rotor PM-MMF can be described as follows (18):

$$F_{PMr}(\theta, t) = \sum_{m=1,3,5,\dots}^{\infty} F_{rm} \sin(mN_r\,(\theta - \omega_r t)) \quad (2)$$

where N_r is the number of rotor slots, ω_r is the angular speed of the rotor, and F_{rm} is the magnitude of the mth harmonic order of the MMF excited by the rotor PMs (F_{PMr}). To calculate the airgap flux density, both the stator and rotor permeances are necessary. The stator permeance function with smoothed rotor iron and slotted stator can be derived as follows (25):

$$\Lambda_s(\theta) = \sum_{i=0,1,2,\dots}^{\infty} \Lambda_{si} \cos(i\frac{N_s}{2}\theta) \quad (3)$$

In addition, the rotor permeance function is obtained with smoothed stator iron while the rotor is slotted (10):

$$\Lambda_r(\theta, t) = \sum_{j=0,1,2,\dots}^{\infty} \Lambda_{rj} \cos(\mathrm{j}\,N_r\,(\theta - \omega_r t)) \quad (4)$$

where Λ_{si} and Λ_{rj} are the magnitudes of the ith and the jth harmonics of the stator and the rotor permeances, respectively. As a result, the airgap flux densities excited by the stator PMs ($B_{ags}(\theta,t)$) and the rotor PMs ($B_{agr}(\theta,t)$) can be written as follows:

$$B_{ags}(\theta,t) = F_{PMs}(\theta)\,\Lambda_r(\theta,t) = \sum_{n=1,3,5,\dots}^{\infty}\sum_{j=0,1,2,\dots}^{\infty}\frac{1}{2}F_{sn}\,\Lambda_{rj}\left[\sin\left((jN_r \pm n\frac{N_s}{2})\theta - jN_r\omega_r t\right)\right] \quad (5)$$

$$B_{agr}(\theta,t) = F_{PMr}(\theta,t)\,\Lambda_s(\theta) = \sum_{m=1,3,5,\dots}^{\infty}\sum_{i=0,1,2,\dots}^{\infty}\frac{1}{2}F_{rm}\,\Lambda_{si}\left[\sin\left((mN_r \pm i\frac{N_s}{2})\theta - mN_r\omega_r t\right)\right] \quad (6)$$

When both the stator PM and rotor PM are taken into account, the no-load airgap flux density can be expressed as follows:

$$B_{ag}(\theta,t) = B_{ags}(\theta,t) + B_{agr}(\theta,t) \quad (7)$$

As can be seen, utilizing the dual-PM excitation in the presented machine gives birth to plenty of airgap flux density harmonics that can play active roles in power conversion. The airgap flux density harmonics can be categorized into four different groups, 1) The harmonics resulted from the interaction between stator PM-MMF components ($n = 1,3,5,\dots$) and the average rotor permeance component ($j = 0$), 2) The harmonics resulted from the interaction between rotor PM-MMF components ($m = 1,3,5,\dots$) and the average stator permeance component ($i = 0$), 3) the modulated harmonics generated by the interaction between stator PM-MMF ($m = 1,3,5,\dots$) and the rotor permeance components ($j = 1,2,3,\dots$), 4) the modulated harmonics generated by the interaction between rotor PM-MMF ($m = 1,3,5,\dots$) and the stator permeance components ($i = 1,2,3,\dots$). More information on the airgap flux density harmonics is included in Table 1.

To validate the above analysis, the airgap flux density waveform and its spectra of a dual-PM AFFRM with 12 stator slots and 13 rotor pole pairs are predicted with the aid of 3-D FEM in the average airgap radius and presented in Figure 3. As it is seen from Figure 3(a), the airgap flux density waveform of the proposed machine, which is the sum of the airgap flux densities produced by the stator and rotor PM MMFs, has unequal positive and negative peaks. This has occurred owing to the CP arrangements of PMs in both the stator and rotor. Figure 3(b) illustrates the harmonic spectra of the airgap flux densities produced by the stator PMs, rotor PMs, and dual-PM. As can be noticed, the dominant harmonics order while considering stator PMs are 6th and 18th, which were earlier categorized under type 1. In addition, the 5th, 7th, 19th, and 31st harmonics belong to the type 3 and 4, and as opposed to type 1, are not static, which means they are responsible for the induction of back-EMF in the windings of the proposed machine. On the other hand, in the case of the rotor PMs, the 13th harmonic is the dominant one, which is classified under type 2. Overall, by employing the dual-PM configuration, the new order of airgap flux density harmonics, such as the 13th emerges, which is absent in the conventional FRPMMs with only stator PMs excitation source. Furthermore, the amplitude of the modulated harmonics, such as the 5th, 7th, 19th, and 31st harmonics, increases, thanks to the rotor PM excitation.

TABLE 1. No-load Airgap Flux Density Harmonics

Pole pairs	Mechanical speed	Type
$n\frac{N_s}{2}$	0	(1)
mN_r	ω_r	(2)
$\left\|jN_r \pm n\frac{N_s}{2}\right\|$	$\frac{jN_r\omega_r}{jN_r \pm n\frac{N_s}{2}}$	(3)
$\left\|mN_r \pm i\frac{N_s}{2}\right\|$	$\frac{mN_r\omega_r}{mN_r \pm i\frac{N_s}{2}}$	(4)

3. DESIGN AND OPTIMIZATION OF THE PROPOSED DUAL-PM AFFRM

3. 1. Design Specifications A three-phase 5.5 kW dual-PM axial-field flux-reversal machine (AFFRM) was designed for a four-wheeler city-commuter electric car.

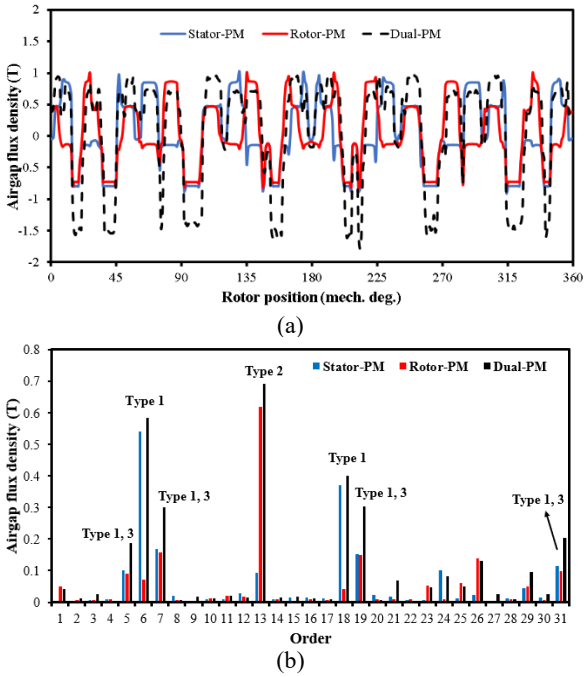

Figure 3. Airgap flux density distribution of the proposed Dual-PM AFFRM. (a) Waveforms. (b) Spectra

The target performance requirements (rated power, torque, and speed) were derived from the drive specifications reported by Kim et al. (30) for a similar class of in-wheel traction systems. For a conventional 225/45R17 tire, the calculated wheel speed at a vehicle speed of 45 km/h corresponds to approximately 380 rpm, which was adopted as the rated speed of the machine. The required torque of 138 Nm was then obtained from the power-speed relationship.

The outer and inner diameters (345.9 mm and 207.5 mm, respectively) and the axial length (78.8 mm) were selected according to the available installation space inside the wheel rim specified by Kim et al. (30). The current density of 5 A/mm² was chosen as a practical limit for liquid-cooled traction machines of this power level to balance copper loss and thermal constraints.

The electromagnetic configuration uses 12 stator slots and 13 rotor poles, a combination shown by Gao et al. (31) to provide a high winding factor (0.933) and nearly sinusoidal back-EMF with low cogging torque. NdFeB magnets with 1.2 T remanence are employed on both stator and rotor sides to achieve high air-gap flux density. The key design parameters are summarized in Table 2. Moreover, the analytical equations for the preliminary design stage are included in the Appendix.

3. 2. Design Optimization Generally, the performance of FRPM machine is highly influenced by multiple design variables (31). Hence, obtaining the desired features requires optimizing the designed model.

TABLE 2. Design Specifications of the Dual-pm AFFRM

Parameters	Value	Unit
Rated power, (P_o)	5.5	Kw
Rated speed, (n_r)	380	rpm
Rated current, ($I_m/\sqrt{2}$)	18	A
Rated voltage, (V_s)	220	V
Outer diameter, (D_o)	345.9	mm
Inner diameter, (D_i)	207.54	mm
Axial length, (l_m)	78.8	mm
Airgap length, (g)	1	mm
Stator yoke height, (h_{ys})	12.6	mm
Stator tooth tip, (h_1)	8	mm
Stator slot height, (h_s)	27	mm
Stator slots, (N_s)	12	-
Rotor pole pairs, (N_r)	13	-
Turns per phase. (n_{ph})	216	Turn
Current density, (J)	5	A/mm^2
Remnenace, (B_r)	1.2	T

Among many methods that have been presented so far, Global optimization based on GA (genetic algorithm) is widely employed to optimize the electromagnetic performances of radial FRPM machines (4, 5, 10). However, the proposed machine has a 3D structure, making its evaluation and optimization costly and a time-consuming task. As a result, to reduce the computational burden significantly and acquire the optimum geometric variable values, the Taguchi approach is chosen in this study and its overall optimization workflow is summarized in Figure 4.

The initial step in the Taguchi method is to set the objectives of the optimization. Since improving the torque characteristics is desirable for In-wheel traction motors, maximizing the average torque is the primary goal of optimization. In addition, to have a smooth operation, minimizing the torque ripple is considered the second goal of optimization in this paper. According to the studies that were conducted on radial FRPM machines, their performance is highly influenced by multiple stator teeth and rotor poles' geometric variables (4, 7, 31). Therefore, in this research, the stator PMs height (H_{PMs}), the rotor PMs height (H_{PMr}), the rotor Iron pole arc θ_{Ri} (elec. deg.), the rotor PM arc θ_{RPM} (elec. deg.) , and the stator slot opening ratio (S_{SO}), which is the ratio of the stator slot opening to the stator slot pitch, are taken as optimization variables (control factors) and shown in Figure 5. Each of the control factors has five levels, which are included in Table 3.

The Taguchi method uses a matrix called orthogonal array in which the impacts of different optimization variables on performance indexes can be evaluated in a limited set of experiments (32). The number of orthogonal array experiments is determined by the number and levels of optimization variables. Considering the optimization variables and their levels, the orthogonal

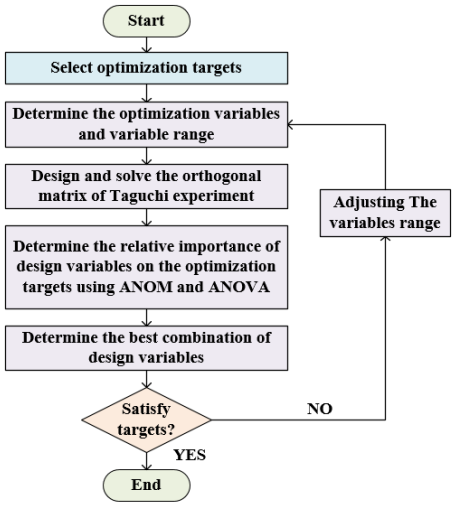

Figure 4. The workflow of implementing Taguchi method

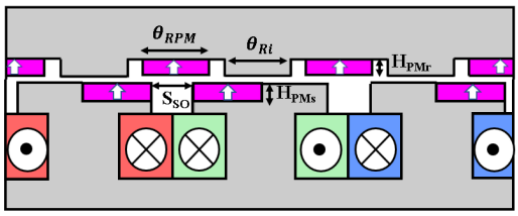

Figure 5. Design variables of the Dual-PM AFRPM machine

TABLE 3. Optimization Variables of the Dual-PM AFFRM

Control factors	Level 1	Level 2	Level 3	Level 4	Level 5
H_{PMs}(mm)	3	3.25	3.5	3.75	4
H_{PMr}(mm)	4	4.25	4.5	4.75	5
θ_{Ri}	126	135	144	153	162
θ_{RPM}	126	135	144	153	162
S_{SO}(%)	0.15	0.2	0.25	0.3	0.35

array of L_{25} is established for this study. The combinations of control factors for each experiment are presented in Table 4. It should be noted that without using the Taguchi method, the number of experiments (3-D simulations) required for the optimization rises to 5^5=3125. This shows that the Taguchi approach is a powerful tool to reduce costs and save time.

After completing all the experiments with the aid of 3-D FEA and obtaining the results, "Analysis of mean (ANOM)" and "Analysis of variance (ANOVA)" are employed to estimate the impacts of control factors on each optimization goal and determine their relative importance (13). The ANOM begins with calculating the average of each objective function as follows (32):

$$Y_m = \sum_{N=1}^{25} Y_N \quad (8)$$

where Y_m, Y_N, N and are the overall mean of an objective function, the value of the objective function at each experiment, and the number of experiments, respectively. In addition, the mean effect of control factors at different levels on objective functions can be calculated as follows (32):

$$Y_{mxk} = \frac{1}{N_L}(Y_{xk}(A) + Y_{xk}(B) + Y_{xk}(C) + Y_{xk}(D) + Y_{xk}(E) \quad (9)$$

where Y_{mxk} and N_L are the average value of the objective function at the k[th] level of the control factor x and the number of control factor levels, respectively. Besides, A, B, C, D, and E indicate the experiments in which a specific control factor is at the k[th] level. The results of the mean control factors' effects on the average torque and torque ripple are illustrated in Figure 6.

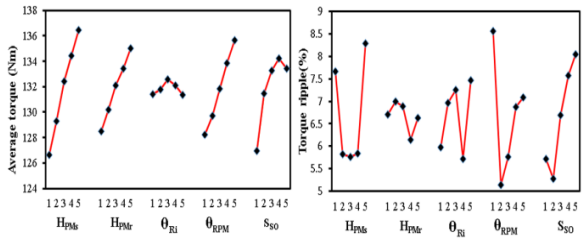

(a) (b)

Figure 6. Mean effects of control factors on (a) average torque (b) torque ripple

TABLE 4. Optimization Variables of the Dual-PM AFFRM

Experiment No	Optimization variables and levels				
	H_{PMs} (mm)	H_{PMr} (mm)	θ_{Ri}	θ_{RPM}	S_{SO} (%)
1	1	1	1	1	1
2	1	2	2	2	2
3	1	3	3	3	3
4	1	4	4	4	4
5	1	5	5	5	5
6	2	1	2	3	4
7	2	2	3	4	5
8	2	3	4	5	1
9	2	4	5	1	2
10	2	5	1	2	3
11	3	1	3	5	2
12	3	2	4	1	3
13	3	3	5	2	4
14	3	4	1	3	5
15	3	5	2	4	1
16	4	1	4	2	5
17	4	2	5	3	1
18	4	3	1	4	2
19	4	4	2	5	3
20	4	5	3	1	4
21	5	1	5	4	3
22	5	2	1	5	4
23	5	3	2	1	5
24	5	4	3	2	1
25	5	5	4	3	2

As can be seen from Figure 5(a), by increasing the levels of control factors H_{PMs}, H_{PMr}, θ_{RPM} and S_{SO} the average torque increases, which is in line with the primary goal of optimization. More specifically, the

combination of the fifth levels of H_{PMs} and H_{PMr}, the third level of θ_{Ri}, the fifth level of θ_{RPM} and the fourth level of S_{SO} maximizes the average torque. However, as shown in Figure 5(b), choosing the third level of H_{PMs}, the fourth level of H_{PMr} and θ_{Ri}, and the second level of θ_{RPM} and S_{SO} is favorable for minimizing the torque ripple. To avoid such a contradiction and obtain the best combination that can simultaneously satisfy both optimization goals, ANOVA is carried out. To reveal the influence share of each control factor on objective functions, the sum of squares (SS) of each control factor for an objective function is calculated using Equation 10, which is presented by Mirnikjoo et al. (32)

$$SS_x = 5\sum_{k=1}^{5}(Y_{mxk} - Y_m)^2 \quad (10)$$

where SSx is the sum of squares of the control factor x The results of the ANOVA analysis are presented in Table 5. As can be deduced, the height of stator PM (H_{PMs}) and rotor PM (H_{PMr}) have larger impacts on the average torque rather than the torque ripple. On the contrary, the proportion influence of the rotor PM arc θ_{RPM}, rotor Iron pole arc θ_{Ri}, and the stator slot opening ratio S_{SO} are larger on the torque ripple. Therefore, based on the calculated control factors effects, the combination with the fifth levels of H_{PMs} and H_{PMr}, the fourth level of θ_{Ri}, the second level of θ_{RPM} and S_{SO} are selected to satisfy both optimization targets simultaneously.

4. EVALUATION OF THE ELECTROMAGNETIC PERFORMANCE OF DUAL-PM AFFRM

4. 1. No-load Condition The no-load flux density distribution and the vector field of the developed motor are depicted in Figure 7. As can be observed, the flux density is in the allowed range in most parts of the machine. However, due to the interpolar flux leakage and the lower magnetic reluctance of the iron poles, partial saturation occurs in the CP areas of the stator. In addition, the airgap flux density waveforms and the corresponding spectra of main-order harmonics in the initial and optimized designs are illustrated in Figure 8. As it is observed, the amplitudes of the main-order airgap flux density harmonics responsible for producing torque increased remarkably due to the optimization.

TABLE 5. Effects of Different Control Factors on Objective Functions

Optimization variables	Average Torque		Torque ripple	
	SS	Factor effect (%)	SS	Factor effect (%)
H_{PMs}	308.05	38.6	30.8	27.77
H_{PMr}	133.53	16.73	2.29	2.06
θ_{Ri}	4.92	0.62	13.08	11.78
θ_{RPM}	180.75	22.65	34.37	30.96
S_{SO}	170.64	21.4	30.44	27.43

Since the flux reversal machines cannot generate the reluctance torque, the cogging torque is the major contributor to torque ripple (12). The cogging torque profiles of the proposed machine in initial and optimized designs are predicted via 3-D FEM and compared in Figure 9. As a result of using the Taguchi method, the peak-to-peak value of cogging torque is reduced from 13.67 Nm to 2.73 Nm in the optimized design. The phase back-EMF of the dual-PM AFFRM is calculated at the rated speed and presented in Figure 10. As it is clear, the amplitude of the fundamental component of the phase back-EMF increased by 10.67% in the optimized model. In addition, the fifth and seventh harmonics are substantially suppressed, leading to a lower torque ripple in the optimized machine.

4. 2. On-load Condition The output torque waveforms of both the initial and optimized designs of the proposed model are illustrated in Figure 11(a).

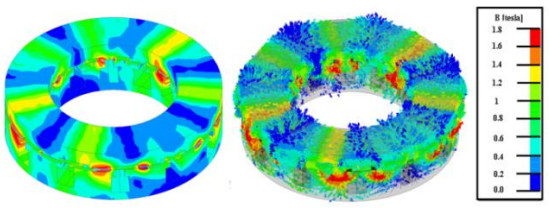

(a) (b)

Figure 7. (a) Flux density distribution of the dual-PM AFFRM (b) Flux vectors of the dual-PM AFFRM

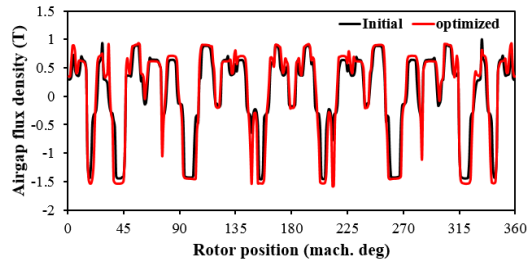

(a)

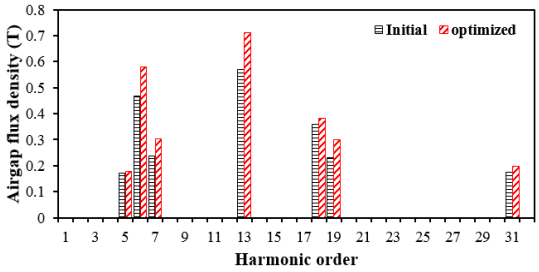

(b)

Figure 8. Airgap flux density distributions of the initial and optimized design. (a) Waveforms. (b) Spectra

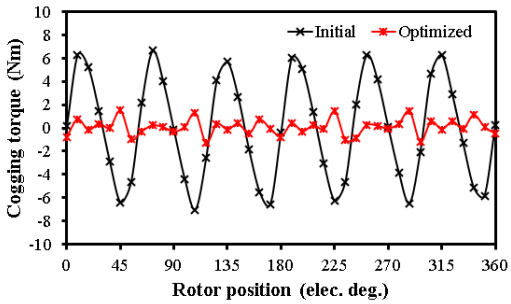

Figure 9. Cogging torque waveforms of the initial and optimized design of the dual-PM AFFRM

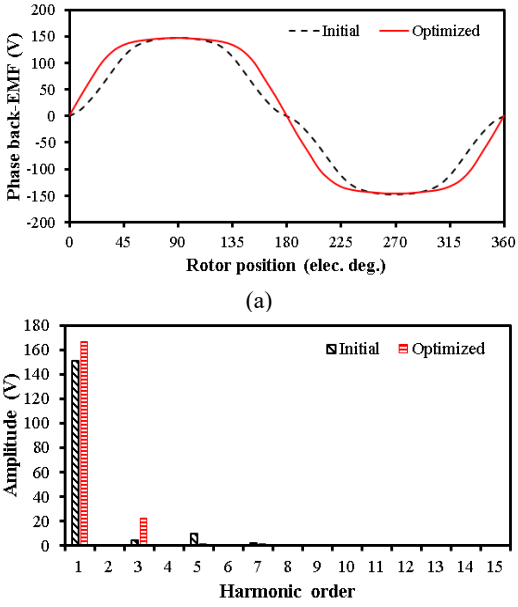

Figure 10. Phase back-EMF in the dual-PM AFFRM (a) Waveform (b) Spectra

Thanks to the Taguchi method, the average torque in the optimized design experienced nearly 10% growth and reached 138.6 Nm. Moreover, the torque ripple decreased from 12.95% to 4.3%. Since the torque ripple is under 5%, it is in the acceptable range for an In-wheel application. Figure 11(b) shows the variations of the average torque with respect to the current angle. It is obvious that, like its radial counterpart, the proposed machine, both in the initial and optimized models, delivers an insignificant reluctance torque that can be neglected. To evaluate the overload capability of the proposed machine, the output torque versus input current curve is depicted in Figure 11(c). As it is seen, the average torque of the proposed machine demonstrates a linear increase over twice the input current. Besides, the optimized model produces a higher torque compared with the initial one over the entire range of input current.

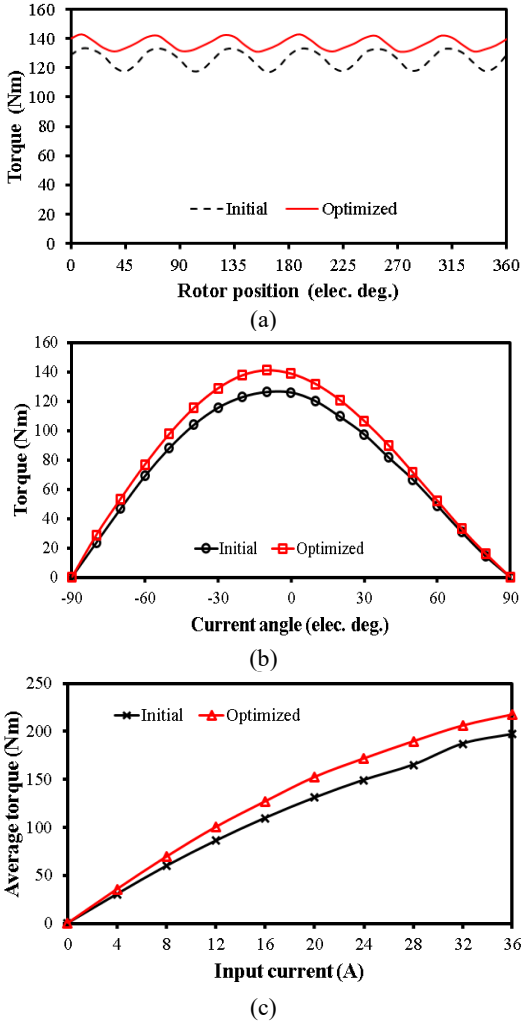

Figure 11. (Torque characteristics of the dual-PM AFFRM. (a) Output torque (b) Torque versus current angle (c) Torque versus input current

4. 3. Flux Weakening Capability According to Qu et al. (10), a K_{fw} factor indicates the field weakening capability of an electric machine and can be expressed as follows:

$$k_{fw} = \frac{L_d I_{rated}}{\Psi_m} \quad (11)$$

Where L_d, Ψ_m, and I_{rated} are the d-axis inductance, PM flux linkage, and the phase rated current. It is preferred k_{fw} to be close to 1 so that the machine has both torque capability in the constant torque region and flux weakening capability in the constant power region (10). For the initial and optimized design, the flux weakening factors are 1.26 and 1.41, respectively. The optimized design shows a figure closer to 1, indicating a better trade-off between the torque and flux weakening capabilities. The values for d and q inductances and PM flux linkages of both models are listed in Table 6.

TABLE 6. Inductances, flux linkages, and flux weakening factors of the initial and optimized designs

	L_d (mH)	L_q (mH)	Ψ_m (mwb)	K_{fw}
Intial	16.08	16.87	321.82	1.26
Optimized	15.95	16.81	289.96	1.41

Figure 12 illustrates the torque-speed and power-speed characteristics of the initial and optimized models. For this purpose, an SVMPWM control strategy with the DC=540 and the maximum allowed current for the windings is employed. As can be observed, both designs can operate over a wide speed range; however, the optimized design exhibits a slightly better performance.

4. 3. Comparison between single-PM AFFRM and dual-PM AFFRM To reveal the impacts of employing dual-PM excitation, the key performance of the proposed machine is compared with a single-PM AFFRM in which PMs are mounted just on the stator, like a conventional radial field FRPMM. It should be mentioned that the torque characteristic of the single-PM AFFRM is optimized using the same method in Section 3. Furthermore, the overall dimensions, input current, number of stator slots, rotor pole pairs, and the number of turns per phase are kept constant for both machines to make a fair analogy. The results of the comparison are tabulated in Table 7. As can be noticed, the average torque of the dual-PM AFFRM is 47% larger compared to its counterpart. As a result, the torque density of the proposed machine grew significantly to 42.92 kNm/m^3 while that of the single-PM AFFRM is 29.19 kNm/m^3. Although the single-PM AFFRM has a lower torque density compared to the dual-PM AFFRM, it ranks higher compared to its radial-flux counterparts developed in the previous studies. In addition, due to the increased number of airgap flux density harmonics in the dual-PM AFFRM, the PM utilization ratio reached 0.54 Nm/cm^3, which is 38.46% higher than in the single-PM AFFRM. Similarly, the power factor of the proposed machine has risen to 0.6 owing to the increase in the airgap flux density harmonics. However, the enriched airgap flux density harmonics led to a higher core loss in the proposed machine. Nevertheless, the dual-PM AFFRM exhibits a higher efficiency compared to its counterpart.

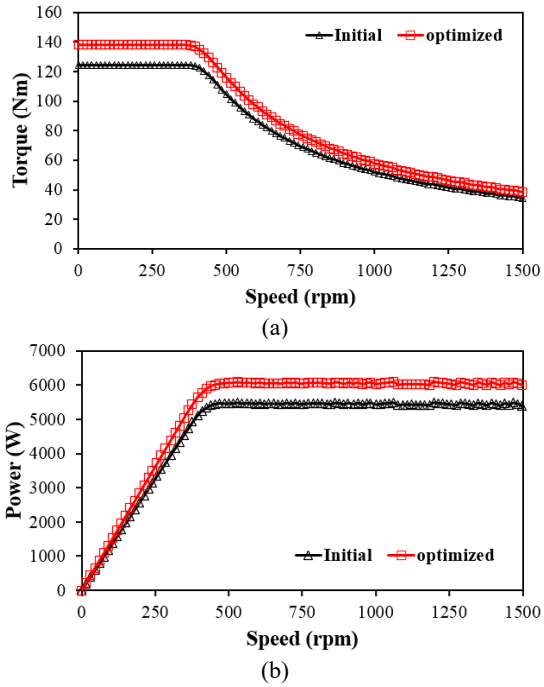

Figure 12. (a) Torque-speed characteristics (b) Power-speed characteristics

5. COMPARATIVE STUDY

Propulsion motors designed for low-speed operation are bulky and heavy. Accordingly, the main concern in In-wheel direct-drive systems is the increased unsprung mass created by the placement of such motors inside the wheel. Therefore, a desirable in-wheel motor must be light and compact, as it simultaneously satisfies other requirements for EV applications. To further investigate the suitability of the proposed motor for in-wheel direct-drive EVs, three different types of high-performance motors designed for low-speed and high-torque applications are chosen from the previous studies for comparison purposes. The candidates are a dual-stator axial-flux spoke-type permanent magnet vernier machine (DS-AFSPMVM) proposed by Zhao et al. (24), indicated by M1 in Table 8, a dual-rotor toroidal winding axial-flux permanent magnet vernier machine (DR-TWAFPMVM) proposed by Zou et al. (23), indicated by M2 in Table 8, and a dual rotor slotless axial-flux permanent magnet

TABLE 7. Comparison of Electromagnetic Performance between Single-PM AFFRM and Dual-PM AFFRM

Items	Single-PM AFFRM	Dual-PM AFFRM
Core loss (W)	56.7	122.6
Copper loss (W)	291.6	
Torque (Nm)	94.3	138.65
Torque ripple (%)	3.57	4.3
Power factor	0.48	0.6
Efficiency (%)	91.5	93
PM volume (cm^3)	244.32	253.355
Torque/PM volume (Nm/cm^3)	0.39	0.54
Torque density (kNm/m^3)	29.19	42.92

synchronous machine (DR-SLAFPMSM) proposed by Si et al. (33), indicated by M3 in Table 8. To draw a fairer analogy, the candidates are chosen to have the operating speed close to that of the proposed motor. In addition, all the motors are air-cooled. As can be seen from Table 8, the torque density of the proposed motor is 13.84%, 31.65%, and 15.22% higher than those of the M1, M2, and M3, respectively. In addition, the torque constant of the Dual-PM AFFRM is 22.22% and 36.52% higher compared to those of the M2 and M3. In terms of efficiency, the proposed motor outperforms both the M1 and M3, while it falls 1.3% below the M2. Another index for comparing the motors is the aspect ratio, which is defined as the ratio of a motor's outer diameter to its axial length. Considering the results, the aspect ratio of the presented motor is remarkably high (4.39). This signifies that the motor has a more pancake shape, which makes it suitable for in-wheel applications. Furthermore, the presented design has a single-sided structure, while other designs have double-sided structures. This indicates that, when it comes to manufacturing complexity and cost, the proposed design is a more attractive candidate in comparison to others.

To have a clearer perspective, some of the best-performed radial-flux FRPMMs are chosen from the previous studies to identify how much the torque density improved in the proposed machine compared to its radial-flux counterparts. The candidates are a dual-PM spoke-type flux reversal machine (dual-PM SFRM) proposed by Wei et al. (25), indicated by M4 in Table 9, an FRPMM with quasi-Halbach array magnets proposed by Qu and Zhu (9), indicated by M5 in Table 9, and a CP-FRPMM proposed by Qu et al. (4), indicated by M6 in Table 9. As before, to make a fair comparison, the candidates are chosen to have a close operating speed to that of the Dual-PM AFFRM. It is seen from Table 8, the torque density of the proposed machine is 16.25%, 16.88%, and 143.86% larger in comparison with those of the M4, M5, and M6, respectively. Also, the proposed model has a considerably higher torque constant than M4 and M6, while it is lower by 15.71% compared to M6. With regard to efficiency, the Dual-PM AFFRM outperforms its other competitors by far. The figures for aspect ratio demonstrate that the Dual-PM AFFRM is more compact than the radial-flux FRPMMs chosen for this study.

Overall, it can be inferred that the Dual-PM AFFRM has a promising performance for In-wheel direct-drive EV applications since it has the largest torque density among the 8 designs.

TABLE 8. Specifications of the proposed, M1, M2 amd M3 motors

Parameters	Proposed	M1	M2	M3
Speed (rpm)	380	300	320	400
Outer diameter (mm)	345.9	334	220	240
Axial length (mm)	78.8	75	91	58
Phase number		3		
Current density (A/mm^2)	5	4.4	5.8	-
Average torque (Nm)	138.65	160.8	106.1	56.44
Torque density (KNm/m^3)	42.92	37.7	32.6	37.25
Torque constant (Nm/A)	7.7	-	6.3	5.64
efficiency	93	86	94.3	84.83
Aspect ratio	4.39	4.45	2.41	4.13

TABLE 9. Specifications of the proposed, M4, M5 amd M6 motors

Parameters	Proposed	M4	M5	M6
Speed (rpm)	380		600	
Outer diameter (mm)	345.9	90	124	90
Axial length (mm)	78.8	25	120	25
Phase number		3		
Current density (A/mm^2)	5	-	-	-
Average torque (Nm)	138.65	5.8	50.1	2.8
Torque density (KNm/m^3)	42.92	36.92	36.72	17.6
Torque constant (Nm/A)	7.7	0.29	9.32	0.53
efficiency	93	85.4	87.2	87.2
Aspect ratio	4.39	3.6	1.03	3.6

5. CONCLUSION

In this study, a dual-permanent-magnet axial-field flux-reversal machine (dual-PM AFFRM) with a single stator and single rotor configuration was presented for in-wheel direct-drive electric vehicle (EV) applications. The operating principle was analyzed using the magnetomotive force (MMF)–permeance model, and the torque characteristics were refined through the Taguchi optimization method to reduce computational effort. After optimization, the average torque increased by approximately 10%, and the torque ripple decreased to 4.3%, which is within a typical range for in-wheel drive systems. Comparative analysis with a single-PM AFFRM showed higher torque density (from 29.19 kNm/m³ to 42.92 kNm/m³) and improved power factor and magnet utilization with the dual-PM structure. Furthermore, benchmarking against several existing axial- and radial-flux machines designed for low-speed, high-torque applications indicated that the proposed configuration provides comparable electromagnetic performance and structural compactness. Overall, the presented design demonstrates the feasibility of the dual-PM AFFRM topology for in-wheel traction applications. Future work will address detailed thermal and mechanical analyses, analytical lifetime estimation, and experimental validation of the proposed concept.

6. APPENDIX

According to the required power for the machine and the application, its overall dimensions are calculated. Based on Huang et al. (34), if the stator resistance and leakage inductance are not considered, the output power of the machine can be defined as follows:

$$P_o = \eta \frac{m}{\mathrm{T}} \int_0^{\mathrm{T}} e(t)\, i(t)\, dt = \eta \frac{m}{2} E_m I_m \quad (12)$$

where η, E_m, I_m, and m are the machine efficiency, the maximum values for EMF and phase current, and the number of phases of the machine, respectively. Assuming the machine is working in the generating mode, the induced EMF in the stator phase winding can be expressed by Equation 13.

$$e(t) = -\frac{d\Psi_m}{dt} = -n_{ph} k_W \frac{d\varphi_m}{d\theta}\frac{d\theta}{dt} = -n_{ph} k_W \frac{d\varphi_m}{d\theta}\omega_r \quad (13)$$

where k_W,Ψ_m, φ_m, and θ are the winding factor, the phase flux linkage created by both PM excitations, the flux linkage of one turn created by both PM excitations, and the rotor angular position, respectively. The phase flux linkage can also be defined as follows:

$$\varphi_m = \varphi_p \cos(N_r \theta) \quad (14)$$

By inserting Equation 14 into Equation 13, the EMF can be rewritten as follows:

$$e(t) = n_{ph} k_W N_r\, \omega_r \varphi_p \sin(N_r\theta) = E_m \sin(N_r\theta) \quad (15)$$

According to Figures 2(b) and 2(d), the maximum flux passing through the stator coil occurs when both PMs on the stator and rotor are aligned with the rotor and stator iron teeth, respectively. In these positions, the area of the airgap (A_g) between the stator and rotor is derived by Equation 16.

$$A_g = \frac{\pi}{8}\left(\frac{w_{PMr}}{N_r} + \frac{w_{PMs}}{N_s}\right)(1 - {k_d}^2)\, {\mathrm{D}_o}^2 \quad (16)$$

In which w_{PMr}, w_{PMs}, and k_d are the ratio of rotor PM width to rotor tooth pitch, the ratio of stator PM width to stator slot pitch, and the ratio of inner diameter to outer diameter of the machine, respectively. Thus, the magnitude of flux per turn can be obtained by Equation 17.

$$\varphi_p = \mathrm{B}_m \frac{\pi}{8}\left(\frac{w_{PMr}}{N_r} + \frac{w_{PMs}}{N_s}\right)(1 - {k_d}^2)\, {\mathrm{D}_o}^2 \quad (17)$$

where B_m is the maximum value of airgap flux density in the no-load condition. By using Equation 17, the E_m can be defined as follows:

$$E_m = n_{ph} k_W N_r \omega_r \mathrm{B}_m \frac{\pi}{8}\left(\frac{w_{PMr}}{N_r} + \frac{w_{PMs}}{N_s}\right)(1 - {k_d}^2)\, {\mathrm{D}_o}^2 \quad (18)$$

The maximum phase current of the machine is related to the stator electrical loading A_s. It can be expressed by the following equation.

$$I_m = \frac{\sqrt{2}\pi A_s}{6\, n_{ph}}\left(\frac{1+k_d}{2}\right)\mathrm{D}_o \quad (19)$$

By inserting Equations 18 and 19 into Equation 12, the output power of the machine can be calculated using Equation 20.

$$P_o = \frac{\sqrt{2}\pi^3}{1920}\eta k_W \mathrm{B}_m A_s n_r \left(w_{PMr} + \frac{w_{PMs}}{N_s}\right)(1 - {k_d}^2)(1 + k_d){\mathrm{D}_o}^3 \quad (20)$$

Also, the output torque of the machine can be obtained by Equation 21.

$$T_o = \frac{\sqrt{2}\pi^2}{64}\eta k_W \mathrm{B}_m A_s \left(w_{PMr} + \frac{w_{PMs}}{N_s}\right)(1 - {k_d}^2)(1 + k_d){\mathrm{D}_o}^3 \quad (21)$$

As it is seen from Figure 13, there are six more geometric design parameters that need to be derived to complete the design process. Hereafter, the equations for the calculation of these design parameters are explained.

If the flux density of the stator yoke (B_{ys}) is fixed, the thickness of the stator yoke can be calculated as below.

$$h_{ys} = \frac{k_d \mathrm{D}_o \mathrm{B}_m}{2\, P_a\, B_{ys}\, K_{stk}} \quad (22)$$

In which P_a and K_{stk} are the stator winding pole pair and the stacking factor of the stator and rotor cores. For the proposed design P_a is calculated via Equation 23.

$$P_a = 3\frac{N_s}{2} - N_r \quad (23)$$

In addition, by assuming the flux density of the stator teeth to be B_{st}, the stator tooth width can be obtained by Equation 24.

$$w_{ts} = \frac{2\, k_d \mathrm{D}_o \mathrm{B}_m}{N_s\, B_{st}\, K_{stk}} \quad (24)$$

To increase the output power/torque and protect the PMs against demagnetization, the stator PMs height ($\mathrm{H_{PMs}}$), rotor PMs height ($\mathrm{H_{PMr}}$) are selected as below:

$$H_{PMs} = H_{PMr} = 4g \sim 6g \quad (25)$$

The optimum ratio for the stator slot opening S_{so} in radial-field FRPMMs is 0.25 (1) and can be calculated by Equation 26. It should be noted that parameters related to the slot area are calculated at the innermost diameter of the stator since the slot area of the stator must be constant in the radial direction.

$$S_{so} = \frac{\pi(k_d \mathrm{D}_o)}{4\, N_s} \quad (26)$$

By using the winding electric loading A_s and the current density J_s, the slot area of the stator can be obtained.

$$A_{slot} = \frac{\pi\, k_d \mathrm{D}_o A_s}{24\, k_f\, J_s} \quad (27)$$

where k_f is the slot filling factor. Also, the stator slot area can be calculated by the stator geometric parameters.

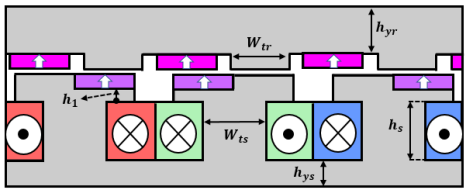

Figure 13. Parametric model of Dual-PM AFFRM

$$A_{slot} = h_s(\frac{\pi\, k_d \mathrm{D}_o}{N_s} - w_t) \quad (28)$$

Equations 27 and 28, the height of the stator slots h_s can be found. Consequently, the axial length of the stator l_s is calculated using Equation 29.

$$l_s = H_{PMs} + h_1 + h_s + h_{ys} \quad (29)$$

Similar to the stator slot calculations, by setting the rotor yoke and teeth flux densities to B_{yr} and B_{rt}, respectively, the rotor yoke height h_{yr} and rotor tooth width w_{tr} are determined as:

$$h_{yr} = \frac{k_d \mathrm{D}_o \mathrm{B}_m}{2\, N_r\, B_{yr}\, K_{stk}} \quad (30)$$

$$w_{tr} = \frac{2\, k_d \mathrm{D}_o \mathrm{B}_m}{N_r\, B_{rt}\, K_{stk}} \quad (31)$$

The rotor length is now calculated by Equation 32.

$$l_r = H_{PMr} + h_{yr} \quad (32)$$

Based on the presented analytical equations, the design of the dual-PM AFFRM can be completed by following the procedure depicted in Figure 14.

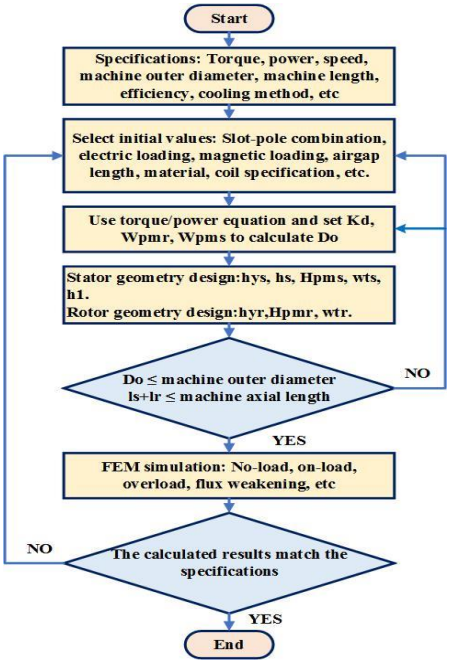

Figure 14. Design flowchart of Dual-PM AFFRM

Funding

The authors declare that no financial support was received for this study.

Declarations Ethics Approval and Consent to Participate

Not applicable. This study did not involve human participants or animals.

Data Availability

All data generated or analyzed during this study are included in this published article.

Declaration of Generative AI and AI-assisted Technologies in the Writing Process

During the preparation of this manuscript, the authors used ChatGPT to improve the clarity of language and to correct grammar. The authors reviewed and edited the content as needed and take full responsibility for the content of the publication.

REFERENCES

1. Gao Y, Qu R, Li D, Li J. Torque performance analysis of three-phase flux reversal machines. IEEE Transactions on Industry Applications. 2017;53(3):2110-9. https://doi.org/10.1109/TIA.2017.2677356
2. Gao Y, Qu R, Li D, Li J, Zhou G. Consequent-pole flux-reversal permanent-magnet machine for electric vehicle propulsion. IEEE Transactions on Applied Superconductivity. 2016;26(4):1-5. https://doi.org/10.1109/TASC.2016.2514345
3. Yang H, Zhu ZQ, Lin H, Li H, Lyu S. Analysis of consequent-pole flux reversal permanent magnet machine with biased flux modulation theory. IEEE Transactions on Industrial Electronics. 2019;67(3):2107-21. https://doi.org/10.1109/TIE.2019.2902816
4. Qu H, Zhu Z, Li H. Analysis of novel consequent pole flux reversal permanent magnet machines. IEEE Transactions on Industry Applications. 2020;57(1):382-96. https://doi.org/10.1109/TIA.2020.3036328
5. Li HY, Zhu Z. Optimal number of magnet pieces of flux reversal permanent magnet machines. IEEE Transactions on Energy Conversion. 2018;34(2):889-98. https://doi.org/10.1109/TEC.2018.2866765
6. Li H, Zhu Z. Influence of adjacent teeth magnet polarities on the performance of flux reversal permanent magnet machine. IEEE Transactions on Industry Applications. 2018;55(1):354-65. https://doi.org/10.1109/TIA.2018.2867818
7. Kim TH. A study on the design of an inset-permanent-magnet-type flux-reversal machine. IEEE Transactions on Magnetics. 2009;45(6):2859-62. https://doi.org/10.1109/TMAG.2009.2018776
8. Xie K, Li D, Qu R, Yu Z, Gao Y, Pan Y. Analysis of a flux reversal machine with quasi-Halbach magnets in stator slot opening. IEEE Transactions on Industry Applications. 2018;55(2):1250-60. https://doi.org/10.1109/TIA.2018.2873540

9. Qu H, Zhu Z. Analysis of spoke array permanent magnet flux reversal machines. IEEE Transactions on Energy Conversion. 2020;35(3):1688-96. https://doi.org/10.1109/TEC.2020.2986948
10. Qu H, Zhu Z, Shuang B. Influences of PM number and shape of spoke array PM flux reversal machines. IEEE Transactions on Energy Conversion. 2020;36(2):1131-42. https://doi.org/10.1109/TEC.2020.3031030
11. More D, Fernandes B. Power density improvement of three phase flux reversal machine with distributed winding. IET Electric Power Applications. 2010;4(2):109-20. https://doi.org/10.1049/iet-epa.2009.0003
12. Li H, Zhu ZQ, Hua H. Comparative analysis of flux reversal permanent magnet machines with toroidal and concentrated windings. IEEE Transactions on Industrial Electronics. 2019;67(7):5278-90. https://doi.org/10.1109/TIE.2019.2934064
13. Wu L, Zheng Y, Fang Y, Huang X. Novel fault-tolerant doubly fed flux reversal machine with armature windings wound on both stator and rotor teeth. IEEE Transactions on Industrial Electronics. 2020;68(6):4780-9. https://doi.org/10.1109/TIE.2020.2989721
14. Zheng Y, Wu L, Zhu J, Fang Y, Qiu L. Analysis of dual-armature flux reversal permanent magnet machines with Halbach array magnets. IEEE Transactions on Energy Conversion. 2021;36(4):3044-52. https://doi.org/10.1109/TEC.2021.3070039
15. Zheng Y, Wu L, Fang Y, Li T, Zheng W. Comparative analysis of doubly fed flux-reversal permanent magnet machines with different PM arrangements and consequent-pole topologies. IEEE Transactions on Magnetics. 2020;57(2):1-6. https://doi.org/10.1109/TMAG.2020.3019821
16. Yu J, Liu C, Zhao H. Design and optimization procedure of a mechanical-offset complementary-stator flux-reversal permanent-magnet machine. IEEE Transactions on Magnetics. 2019;55(7):1-7. https://doi.org/10.1109/TMAG.2019.2896177
17. Aslani B, Gholamian S, Abdollahi SE. Analysis of a double stator flux reversal permanent magnet machine with Halbach array magnets. In: 14th Power Electronics, Drive Systems, and Technologies Conference (PEDSTC); 2023. p. 1-6. https://doi.org/10.1109/PEDSTC57673.2023.10087099
18. Meng Y, Fang S, Wang H, Pan Z, Qin L. Design and analysis of a new dual-stator consequent-pole flux reversal machine with triple-PM excitation. IEEE Transactions on Magnetics. 2021;57(6):1-4. https://doi.org/10.1109/TMAG.2021.3070855
19. Meng Y, Fang S, Pan Z, Liu W, Qin L. Design and analysis of a new partitioned stator hybrid-excited flux reversal machine with dual-PM. IEEE Transactions on Magnetics. 2021;58(2):1-6. https://doi.org/10.1109/TMAG.2021.3077035
20. Wu Z, Zhu Z. Partitioned stator flux reversal machine with consequent-pole PM stator. IEEE Transactions on Energy Conversion. 2015;30(4):1472-82. https://doi.org/10.1109/TEC.2015.2448796
21. Zhu ZQ, Wu ZZ, Evans DJ, Chu WQ. Novel electrical machines having separate PM excitation stator. IEEE Transactions on Magnetics. 2014;51(4):1-9. https://doi.org/10.1109/TMAG.2014.2358199
22. Wu Z, Zhu Z, Zhan H. Comparative analysis of partitioned stator flux reversal PM machines having fractional-slot nonoverlapping and integer-slot overlapping windings. IEEE Transactions on Energy Conversion. 2016;31(2):776-88. https://doi.org/10.1109/TEC.2016.2525826
23. Zou T, Li D, Qu R, Li J, Jiang D. Analysis of a dual-rotor, toroidal-winding, axial-flux vernier permanent magnet machine. IEEE Transactions on Industry Applications. 2017;53(3):1920-30. https://doi.org/10.1109/TIA.2017.2657493
24. Zhao F, Lipo TA, Kwon BI. A novel dual-stator axial-flux spoke-type permanent magnet vernier machine for direct-drive applications. IEEE Transactions on Magnetics. 2014;50(11):1-4. https://doi.org/10.1109/TMAG.2014.2329861
25. Wei F, Zhu Z, Qu H, Yan L, Qi J. New dual-PM spoke-type flux-reversal machines for direct-drive applications. IEEE Transactions on Industry Applications. 2022;58(5):6190-202. https://doi.org/10.1109/TIA.2022.3190248
26. Zhao J, Wang Q, Han Q. Reducing torque ripple through innovative configuration of permanent magnet based on air gap field modulation theory in a novel axial flux reversal permanent magnet machine. IEEE Access. 2024;12:54901-12. https://doi.org/10.1109/ACCESS.2024.3389699
27. Patel A, Suthar B. Design optimization of axial flux surface mounted permanent magnet brushless DC motor for electrical vehicle based on genetic algorithm. International Journal of Engineering, Transactions A: Basics. 2018;31(7):1050-6. https://doi.org/10.5829/ije.2018.31.07a.07
28. Quoc VD, Huu HB. Modeling of surface-mounted permanent magnet synchronous motors with inner and outer rotor types. International Journal of Engineering, Transactions C: Aspects. 2024;37(12):2529-37. https://doi.org/10.5829/ije.2024.37.12c.11
29. Conga TT, Vua TN, Minha DB, Thanhc HV, Quoc VD. Analytical modelling of a six-phase surface mounted permanent magnet synchronous motor. International Journal of Engineering, Transactions A: Basics. 2024;37(7):1274. https://doi.org/10.5829/ije.2024.37.07a.07
30. Kim JH, Choi W, Sarlioglu B. Closed-form solution for axial flux permanent-magnet machines with a traction application study. IEEE Transactions on Industry Applications. 2015;52(2):1775-84. https://doi.org/10.1109/TIA.2015.2496877
31. Gao Y, Qu R, Li D, Li J, Wu L. Design of three-phase flux-reversal machines with fractional-slot windings. IEEE Transactions on Industry Applications. 2016;52(4):2856-64. https://doi.org/10.1109/TIA.2016.2535108
32. Mirnikjoo SA, Abbaszadeh K, Abdollahi SE. Multiobjective design optimization of a double-sided flux switching permanent magnet generator for counter-rotating wind turbine applications. IEEE Transactions on Industrial Electronics. 2020;68(8):6640-9. https://doi.org/10.1109/TIE.2020.3005106
33. Si J, Zhang T, Hu Y, Gan C, Li Y. An axial-flux dual-rotor slotless permanent magnet motor with novel equidirectional toroidal winding. IEEE Transactions on Energy Conversion. 2021;37(3):1752-63. https://doi.org/10.1109/TEC.2021.3138465
34. Huang S, Luo J, Leonardi F, Lipo TA. A comparison of power density for axial flux machines based on general purpose sizing equations. IEEE Transactions on Energy Conversion. 1999;14(2):185-92. https://doi.org/10.1109/60.766982

Persian Abstract

چکیده

این مقاله یک ماشین جدید شاربرگردان با میدان محوری و آهنربای دائم دوگانه (Dual-PM AFFRM) دارای یک استاتور و یک روتور برای کاربرد در خودروهای الکتریکی درون‌چرخی محرک مستقیم (Direct-drive In-wheel) ارائه می‌دهد. توپولوژی و اصول عملکردی ماشین توضیح داده شده است و تأثیرات استفاده از آهنربای دائم دوگانه بر هارمونیک‌های چگالی شار فاصله هوایی با استفاده از یک مدل ساده نیروی محرکه مغناطیسی –پرمانس آشکار شده است. برای به دست آوردن مشخصه گشتاور بهینه ماشین و کاهش حجم محاسباتی، از روش تاگوچی استفاده شده است. عملکرد الکترومغناطیسی طراحی بهینه شده از طریق روش المان محدود سه‌بعدی ارزیابی شده است. نتایج نشان می‌دهند که ماشین بهینه شده قابلیت گشتاور بالا، ریپل گشتاور کم و قابلیت تضعیف شار خوب را ارائه می‌دهد. علاوه بر این، نتایج یک مطالعه مقایسه‌ای بین هشت ماشین کششی مختلف نشان می‌دهد که ماشین جدید شاربرگردان با میدان محوری و آهنربای دائم دوگانه، بالاترین چگالی گشتاور را با نسبت وجه بالا و ثابت گشتاور بالا ارائه می‌دهد که برای کاربردهای خودروهای الکتریکی درون‌چرخی محرک مستقیم بسیار مهم هستند.